Materials Science in Semiconductor Processing 217 (2027) 111125

Contents lists available at ScienceDirect

Materials Science in Semiconductor Processing

journal homepage: www.elsevier.com/locate/mssp

Electron-beam direct writing-based fabrication of high-performance carbon-based dielectrics towards all-carbon electronics

Rui Li [a,b,c], Hao Tian [a], Kaicheng Yu [a], Cao Tang [a], Kaiming Zhang [a], Luzhen Hao [a], Xin He [a], Yanqing Ma [a,b,c,d], Lei Ma [a,b,c,*]

[a] Tianjin International Center for Nanoparticles and Nanosystems, Tianjin University, Tianjin, 300072, PR China
[b] Tianjin Key Laboratory of Low-dimensional Electronic Materials and Advanced Instrumentation, Tianjin, 300072, PR China
[c] Haihe Laboratory for Low-dimensional Electronic Materials, Add 1 to No. 57 Wujiayao Street, Hexi District, Tianjin, 300074, PR China
[d] School of Precision Instrument and Opto-electronics Engineering. Tianjin University, Tianjin, 300072, PR China

ARTICLE INFO

Keywords:
Electron-beam direct writing
Carbon-based dielectric
All-carbon circuit
Graphene field-effect transistor

ABSTRACT

Silicon-based integrated circuits face performance bottlenecks due to inherent material and processing limitations. Low-dimensional carbon-based materials, including graphene and carbon nanotubes, offer promising routes toward next-generation high-performance, low-power integrated circuits. However, current all-carbon circuits still rely on dielectric layers inherited from silicon technology, which limit full compatibility and overall circuit performance. Here, we report a carbon-based dielectric layer fabricated via direct electron-beam lithography of AZ5214 photoresist and systematically investigate the influence of key processing parameters. XPS reveals a predominantly sp^3-hybridized carbon network (64%) with minimal sp^2 fraction (2.04%) and substantial oxygen functionalities (~34%), providing the chemical basis for its insulating behavior. The optimized dielectric exhibits a leakage current density of 7.8×10^{-7} A cm^{-2} at 7.3 MV cm^{-1}, a breakdown field of 7.4 MV cm^{-1}, and frequency-stable response up to 5 MHz,which is well below the typical tolerance levels for most electronic device applications. When employed as the gate insulator in top-gated graphene FETs (with metal contacts and gate electrode), it achieves a carrier mobility of 2607 cm^2 V^{-1} s^{-1} alongside a dielectric constant of ~5.4. Notably, the electron-beam approach integrates material formation and patterning into a single step, eliminating the need for seed layers, high-temperature annealing, or additional lithography. These combined advantages—a clean graphene/dielectric interface, process simplicity, and balanced electrical properties—render this dielectric not only suitable for practical graphene-based top-gated integrated circuits, but also an attractive candidate for serving as the insulating layer in future all-carbon electronics.

1. Introduction

Since the 1960s, Moore's Law has propelled the swift evolution of silicon-based integrated circuit technology, profoundly influencing modern life [1,2]. As chip technology advances, there has been a continued scaling of device dimensions, leading to enhanced device performance and chip integration. Nonetheless, scaling down of silicon-based transistors is approaching the physical limitations of both materials and fabrication processes. Furthermore, manufacturing processes have become increasingly sophisticated, thereby elevating the costs of both design and process. Challenges such as power walls [3], storage walls [4], and scaling issues are hindering the ongoing advancement of Moore's Law [5]. In an effort to overcome these limitations, the scientific community has shifted its focus towards carbon-based materials [6]. Graphene [7–10] and carbon nanotubes [11,12], lauded for their high carrier mobility, ultra-thin channels, and compatibility with existing silicon-based CMOS technology, are predicted to serve as the foundational materials for a new generation of high-performance, low-power chips [13,14].

Current all-carbon circuits predominantly utilize graphene or carbon nanotubes as channels and/or functional materials. For electrodes and interconnects, conductive carbon materials such as multilayer graphene or amorphous carbon are fabricated using various techniques [15–18]. Nevertheless, the dielectrics in these circuits still largely rely on conventional materials adapted from silicon-based CMOS processes [19,20], including inorganic oxides like Al_2O_3 [21] and certain polymer

* Corresponding author. Tianjin International Center for Nanoparticles and Nanosystems, Tianjin University, Tianjin, 300072, PR China.
E-mail address: lei.ma@tju.edu.cn (L. Ma).

https://doi.org/10.1016/j.mssp.2026.111125
Received 3 June 2026; Received in revised form 18 August 2026; Accepted 28 August 2026
Available online 3 September 2026

dielectrics [22,23]. Significant challenges stem from the poor compatibility and performance degradation observed when growing conventional dielectrics on carbon-based channels, alongside the stringent requirements posed by polymer alternatives [24–28]. These limitations impede the full exploitation of the intrinsic advantages offered by all-carbon systems:most notably, the high-quality, low-defect interfaces formed between homogeneous or similar carbon materials, which facilitate highly efficient carrier transport [29]. Therefore, to advance the development of all-carbon circuits, it is essential to establish a straightforward, stable, and materially compatible fabrication process for carbon-based dielectrics.

Among the various methods currently available for the synthesis of carbon-based materials, electron-beam direct writing stands out due to its high resolution, low power consumption, and capability for pattern definition [30,31]. Specifically, the resolution of electron-beam direct writing can reach a few nanometers, enabling the fabrication of patterns that meet the demands for device miniaturization and high integration. Moreover, compared to alternative techniques, electron-beam writing significantly reduces the processing time for carbon-based materials and streamlines electrode fabrication. In addition, this technique offers a "write-and-inspect" functionality, integrating material deposition with in situ characterization. Under electron-beam irradiation, photoresists can follow distinct transformation pathways depending on processing conditions [32]. Prevailing studies have focused on removing hydrogen and oxygen to yield conductive amorphous or graphitic carbon [33–35]. In contrast, the formation of insulating, device-compatible carbon dielectrics-a key enabler for monolithic all-carbon circuits-has received little attention.

In this work, we propose a method for preparing a carbon-based dielectric via electron-beam direct writing of AZ5214 photoresist and systematically investigate the effects of key processing parameters. The optimized dielectric exhibits low leakage current, which is well below the typical tolerance levels for most electronic device applications. A graphene top-gated field-effect transistor (FET, with metal contacts and gate electrode) employing this carbon-based dielectric as the gate insulator achieves high carrier mobility and a favorable balance between insulating capability and transport performance, which makes this gate dielectric a promising candidate for practical graphene-based top-gated FETs, and further suggest its potential as an excellent insulating layer for future all-carbon integrated circuits.

2. Experimental section

Fig. 1a illustrates the fabrication process of the carbon-based dielectric using electron-beam direct writing. 1) The AZ5214 photoresist was first diluted in isopropanol to adjust the carbon source concentration, and then spin-coated onto SiO_2/Si substrates at 4000 rpm for 40 s. 2) A copper film was subsequently deposited onto the photoresist layer by sputtering to serve as a catalyst. The presence of copper facilitates the fracture of C–C and C–H bonds within the AZ5214 photoresist

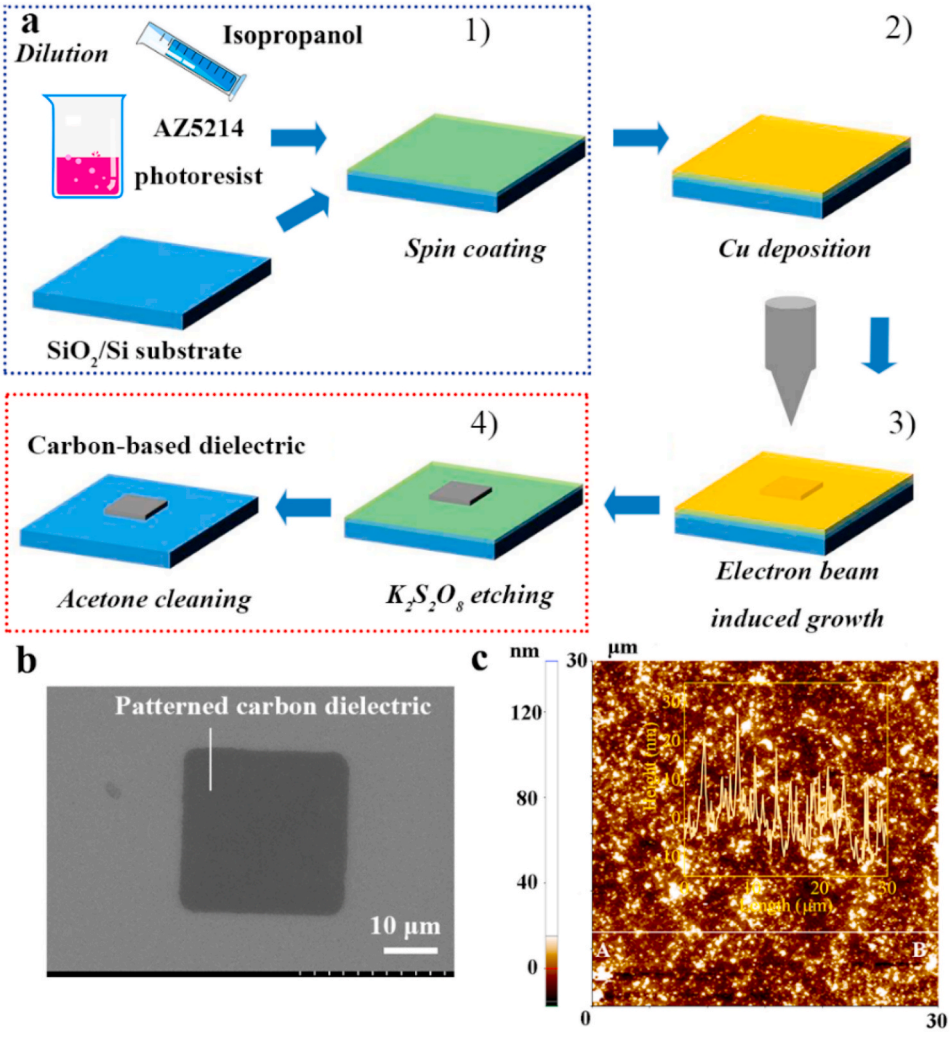

Fig. 1. a) Schematic diagram of the preparation process of carbon-based dielectrics grown by electron-beam direct writing. b) SEM and c) AFM result of patterned carbon-based dielectric layer.

upon electron-beam irradiation [36–39], thereby accelerating the first phase of the growth process (Phase 1, Fig. 2a), as discussed later. 3) The AZ5214 thin film was converted into a carbon-based dielectric using a focused electron beam in an electron-beam lithography (EBL) system, with an acceleration voltage ranging from 10 to 30 kV and an electron-beam dose between 100 and 5000 C/m^2 4) The copper film was then etched away using a saturated potassium persulfate solution, followed by an acetone rinse to ensure complete removal of the untransformed photoresist. Fig. 1b and c shows the SEM and AFM result of patterned carbon-based dielectric layer, which roughness $S_q = 7.8$ nm. The fabrication process began with electron-beam lithography (EBL) using a TECAN VAGE3 system for direct writing of the desired patterns. The chemical composition and elemental states of the films were investigated by X-ray photoelectron spectroscopy (XPS, pHI 2510 XPS system). The thickness and surface roughness of the resulting samples were characterized by atomic force microscopy (AFM, NX-10, Park), while the structural properties of the carbon-based dielectric were examined using Raman spectroscopy (Raman, RTS-2, Titan Electro-Optics). The insulating performance of the samples was evaluated using two electrical characterization systems: a Qianye probe station equipped with a Keithley 2450 sourcemeter, and a Lake Shore TTPX probe station coupled with a Keysight B1500A semiconductor parameter analyzer.

3. Results and discussion

3.1. Systematic investigation of the growth mechanism and key processing parameters for carbon-based dielectrics fabricated via electron-beam writing

The preparation of carbon-based dielectrics by electron-beam direct writing mainly includes two phases, as shown in Fig. 2a. In phase 1, the AZ5214 hydrocarbon undergoes molecular chain fragmentation from large to small under high-intensity electron beam irradiation. As decomposition proceeds, the liberated oxygen and hydrogen atoms combine to form volatile groups such as CO_2, H_2, and CH_3O [40,41]. In phase 2, as the dose of the electron beam increases, the AZ5214 photoresist converts from a positive to a negative tone due to the enhanced crosslinking of its small molecular chains [42–45]. Limited by the maximum electron-beam acceleration voltage in our experiment, the electron-beam energy is insufficient to directly carbonize the photoresist. Therefore, the extent of the aforementioned small molecular chain crosslinking can be controlled by modulating other parameters (e.g., the electron-beam dose and the AZ5214 content), thereby regulating the insulating properties of the final carbon-based dielectrics.

Variations in the thickness of the carbon-based dielectrics indirectly reflect the aforementioned growth process. As shown in Fig. 2b, the thickness of the carbon-based dielectrics prepared under different AZ5214 contents changes with the electron-beam dose. It can be found that as electron-beam dose increases, the thickness of the carbon-based dielectrics initially increases and then plateaus, indicating that a sufficient dose of electron beam is required to provide the energy necessary to fragment large molecular chains into small ones (phase 1) and then crosslink them into a negative-tone network (phase 2), until the photoresist is fully converted (Fig. 2b plateaus). Moreover, a higher AZ5214 content results in a thicker carbon-based dielectric, owing to the greater total volume of large molecules in it. Fig. 2c presents the AFM height image of the carbon dielectric layer for thickness determination. For each sample, five different locations were measured to obtain a comprehensive assessment of the sample height.

To quantitatively evaluate the efficiency of the electron-beam-induced transformation, we derived the dose sensitivity from the slope of the thickness–dose curves shown in Fig. 2b. This parameter represents the incremental change in film thickness per unit electron-beam dose, with units of nm·cm^2/C (equivalently, nm per C/cm^2). As shown in Fig. 2d, the dose sensitivity varies significantly with AZ5214 concentration. For the 600 μL samples, the sensitivity reaches a maximum of 0.015 nm m^2/C at a dose of 100 C/m^2, beyond which it gradually decreases. This decrease can be attributed to the saturation of crosslinking and carbonization reactions at high doses, where additional electron exposure primarily induces structural densification rather than further thickness growth. In contrast, the 1000 μL samples exhibit a higher peak sensitivity of 0.058 nm m^2/C, consistent with the higher carbon content in the precursor film, which provides more available reaction sites for electron-beam-induced crosslinking.

To substantiate the aforementioned process, Raman spectra were recorded for the carbon-based dielectrics fabricated by electron-beam direct writing using AZ5214 at varying content (laser wavelength 532 nm,acquisition time 5 s, laser power 80 mW and the baseline correction procedure) as illustrated in Fig. 2c. In contrast to the Raman signal of the pristine AZ5214 photoresist, the carbon-based dielectric prepared after electron-beam irradiation exhibited D peak (~1350 cm^{-1}) and G peak (~1580 cm^{-1}) signals, consistent with the negative conversion of photoresists to amorphous carbon reported in a previous study [46,47]. A higher AZ5214 content yielded a more intense Raman signal, validating that a greater amount of photoresist could undergo more carbonized conversion. To further elucidate the chemical composition and bonding states of the electron-beam-writing 1500 μL AZ5214 films, XPS measurements were performed. The survey spectrum (Fig. 2f–up) reveals that the films are composed exclusively of carbon (76.84 at%) and oxygen (23.16 at%), confirming the formation of a carbonaceous material with high purity and substantial functionalization. The high-resolution C 1s spectrum (Fig. 2f, down) was deconvoluted into four components after charge correction (calibrated to the adventitious carbon peak at 284.8 eV): sp^2 C–C at 284.2 eV (2.04%), sp^3 C–C/C–H at 285.1 eV (64.00%), C–O at 286.3 eV (22.94%), and C=O at 288.4 eV (11.02%). The overwhelming dominance of sp^3 carbon (64%) and the negligible sp^2 fraction (2.04%) indicate that the carbon network is predominantly composed of tetrahedral carbon with virtually no extended π-conjugation. The sp^3/sp^2 ratio of approximately 31.4 confirms an extremely high degree of structural disorder, which is further corroborated by the significant oxygen content (23.16 at%) and oxygen-containing functional groups (34% of carbon species). Collectively, these characteristics—the sp^3-dominated carbon framework, the absence of π-conjugated pathways, and the presence of polar oxygen functionalities—provide a clear and consistent explanation for the excellent insulating behavior of our carbon-based dielectric. This interpretation is fully supported by the Raman D/G bands (Fig. 2e) and the O 1s spectrum (Fig. S3), which shows a single peak at 532.2 eV corresponding to C–O and C=O species.

To evaluate the electrical properties of the carbon-based dielectric, we fabricated metal–insulator–metal (MIM) capacitors using the electron-beam-treated AZ5214 films as the insulating layer. Fig. 2g shows an optical microscopy image of a typical MIM device, with the equivalent circuit diagram inset. In this structure, the carbon-based dielectric is sandwiched between a 20 nm Cr/20 nm Au bottom electrode and a 20 nm Cr/20 nm Au top electrode. This MIM configuration was used for all leakage current (Fig. 2h–j, Fig. 3e) and capacitance measurements (Fig. 3b and c) presented in this work.

Fig. 2h shows the leakage current density of carbon-based dielectrics obtained at different AZ5214 contents under different electron-beam doses, with a 30 kV electron-beam acceleration voltage and fixed 2.5 MV/cm electric field. As the electron-beam dose increases, the leakage current density of the carbon-based dielectrics decreases. Moreover, the carbon-based dielectrics prepared from a higher AZ5214 content exhibit a lower leakage current density. This confirms that a sufficient electron-beam dose and a high AZ5214 content can result in a carbon-based dielectric with excellent insulation performance. However, as evident from the curve corresponding to a 1000-μL AZ5214 content, beyond a certain level of electron-beam dose and AZ5214 content, the extent of further reduction in leakage current density diminishes. This warrants further exploration.

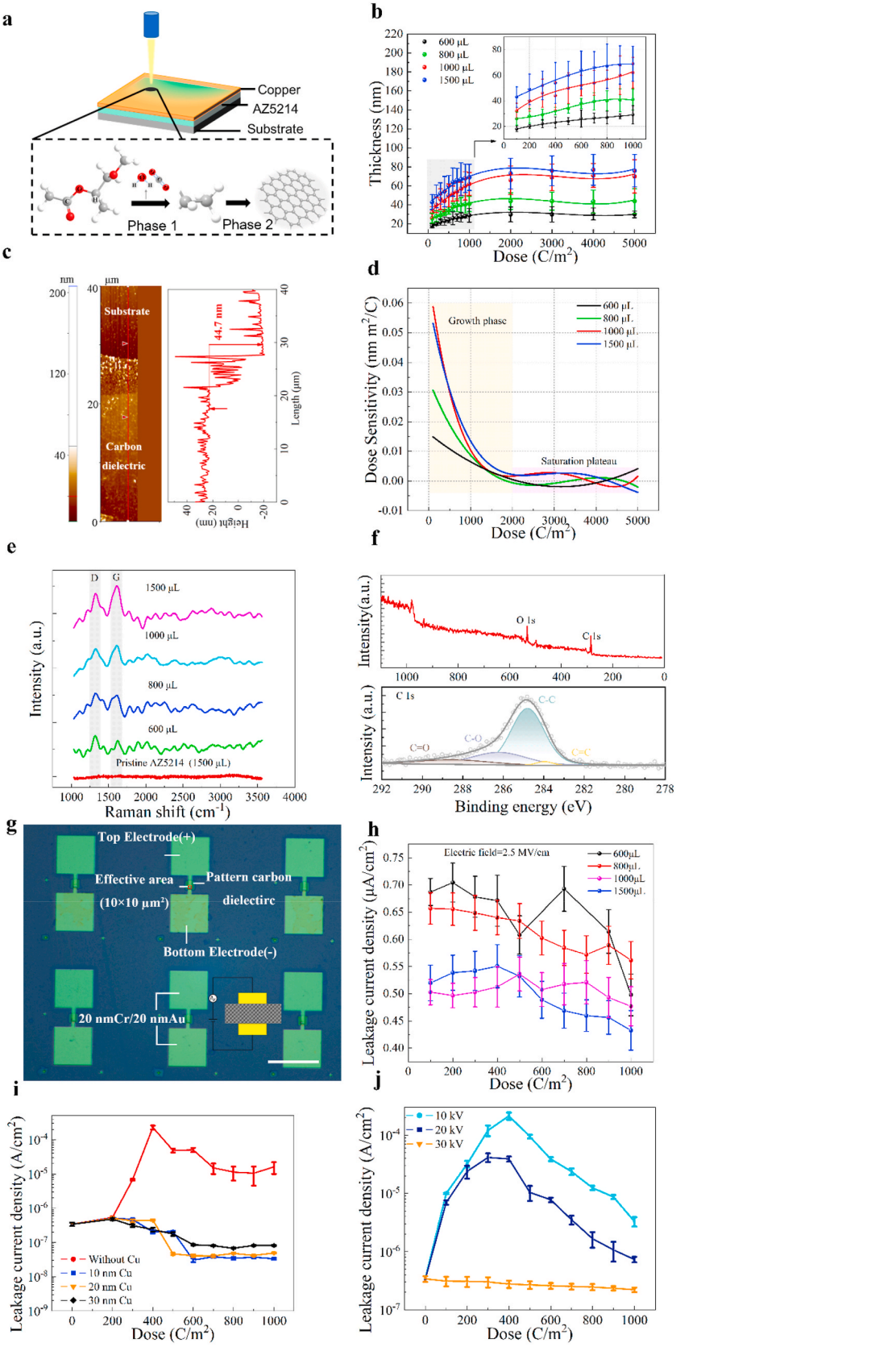

(caption on next page)

Fig. 2. a) Schematic diagram of the growth principle of carbon-based dielectrics fabricated by electron-beam direct writing of AZ5214 photoresist. b) Thickness of carbon-based dielectrics as a function of electron-beam dose for different AZ5214 content. The inset provides an enlarged view over the dose interval from 0 to 1000 C/m^2 c) AFM height image of the carbon dielectric layer, with thickness determined from the step height across the pattern edge. d) Dose sensitivity as a function of electron-beam dose for different AZ5214 content, calculated from the slope of the thickness–dose curves in b to represent the incremental thickness change per unit dose (nm·m^2/C). e) Raman spectra of carbon-based dielectrics grown at different AZ5214 content, showing the characteristic D and G bands of disordered carbon. f) XPS characterization of the electron-beam-written AZ5214 film. Upper panel: survey spectrum showing C 1s and O 1s peaks with atomic concentrations of 76.84% and 23.16%, respectively. Lower panel: high-resolution C 1s spectrum deconvoluted into sp^2 C (284.2 eV, 2.04%), sp^3 C (285.1 eV, 64.00%), C–O (286.3 eV, 22.94%), and C=O (288.4 eV, 11.02%). g) Schematic diagram and an typical optical image of the MIM structures, with current flowing from the top electrode to the bottom electrode; Scale bars: 100 μm in the optical image. h) Leakage current density as a function of electron-beam dose for different AZ5214 content, measured at a fixed electric field of 2.5 MV/cm i) Electron-beam-dose dependence of leakage current density for carbon-based dielectrics fabricated with varying copper film thickness (1000 μL AZ5214, 30 kV acceleration voltage). j) Electron-beam-dose dependence of leakage current density for carbon-based dielectrics fabricated with varying electron-beam acceleration voltages (1000 μL AZ5214, 30-nm-thick copper film).

Fig. 2i and j demonstrate the impacts of copper film thickness (at a fixed 30-kV acceleration voltage) and electron-beam acceleration voltage (at a fixed 10-nm copper thickness), respectively, on the leakage current density of the carbon-based dielectrics. In Fig. 2i, it can be seen that under the preparation condition without copper and no electron-beam direct writing (0 C/m^2), the leakage current density of AZ5214 positive photoresist is about 3.4×10^{-7} A/cm^2. The transformation from AZ5214 positive to negative photoresist is achieved at 400 C/m^2, and due to incomplete transformation, its leakage current density is extremely high ($\sim 2.3 \times 10^{-4}$ A/cm^2). When the electron-beam dose is further increased to 700 C/m^2, the leakage current density of the carbon-based dielectrics no longer decreases with the increase of electron-beam dose ($\sim 1.5 \times 10^{-5}$ A/cm^2), indicating that the conversion of AZ5214 in the absence of copper has reached its limit. When preparing carbon-based dielectrics with copper films, the carbonized conversion deepens, and the leakage current density decreases ($\sim 3.3 \times 10^{-8}$ A/cm^2) with the enhancement of electron-beam dose. In addition, the increase in copper thickness leads to an increase in the leakage current density of the prepared dielectric layer, possibly due to the dissipation of a portion of the electron-beam energy through scattering and reflection by the relatively thick copper.

As indicated in Fig. 2j, an electron-beam acceleration voltage below 30 kV is insufficient to drive adequate negative-tone crosslinking of AZ5214 photoresist at the given content, thereby resulting in a relatively high overall leakage current density. Moreover, the initial rise and subsequent fall in the leakage current density indicate a conversion of the AZ5214 photoresist from a positive to a negative tone. Once the electron-beam acceleration voltage reaches 30 kV, the maximum negative-tone crosslinking at any given electron-beam dose can be attained. Consequently, a copper film with an appropriate thickness (10 nm) and a sufficiently high electron-beam acceleration voltage (30 kV) are required to ensure the maximum negative-tone conversion of the AZ5214 photoresist, thereby minimizing the leakage current density of the carbon-based dielectrics.

3.2. Investigation of electronic properties of carbon-based dielectrics

In order to apply the prepared carbon-based dielectrics to all-carbon devices and circuits, the equivalent circuit diagram and the optical microscopy image (OM) correspond to the same metal-insulator-metal (MIM) test structure as that depicted in Figs. 2g and 3a, consists of a patterned carbon-based dielectric encapsulated by two electrodes (Cr: 20 nm/Au: 20 nm).

To gain further insight into the dielectric behavior and interface quality of the carbon-based films, we performed systematic capacitance–voltage (C–V) measurements on the MIM capacitors under various conditions. Fig. 3b shows the C–V curves measured at 10 kHz over a voltage range of −1 V to +1 V for both 1000 μL and 1500 μL samples with different dielectric thicknesses. For the 1500 μL samples, the capacitance density ranges from 64 to 69 nF/cm^2, while for the 1000 μL samples, it ranges from 53 to 56 nF/cm^2. Importantly, all C–V curves in Fig. 3b exhibit flat responses with negligible voltage dependence over the entire measured range, regardless of the AZ5214 concentration or film thickness. This observation indicates the absence of significant charge trapping, mobile ions, or interface states at the electrode–dielectric interface. In conventional dielectric materials, voltage-dependent capacitance often arises from trap-mediated charge injection or polarization saturation under high electric fields, which can severely degrade device performance. The flat C–V characteristics of our carbon-based dielectric therefore confirm the good quality of the MIM capacitors and the stability of the dielectric under applied bias, making it suitable for reliable device operation.

To further evaluate the frequency stability of the dielectric response, we measured the C–V characteristics at frequencies from 10 kHz to 5 MHz under ±1 V (Fig. 3c). The capacitance density remains essentially constant across the entire frequency range for both 1000 μL and 1500 μL samples, with no observable dispersion or relaxation. This frequency-independent behavior indicates that the oxygen-containing functional groups are covalently bonded within the rigid sp^3-dominated carbon network, rather than existing as mobile polar side chains that would exhibit dipolar relaxation. The capacitance density scales with the AZ5214 content, consistent with the higher carbon density in the 1500 μL precursor. The combination of voltage-independent and frequency-stable capacitance is advantageous for practical device applications, ensuring predictable performance under varying bias and operating frequencies up to 5 MHz. These results establish the electron-beam-treated AZ5214 carbon-based dielectric as a promising candidate for high-frequency electronic applications. The capacitance C is related to the dielectric constant k through the following relationship [53]:

$$C = \frac{A\varepsilon_0 k}{t_{ox}}$$

Where A is the effective overlap area of the electrodes of the MIM structure, t_{ox} is the thickness of the carbon-based dielectric, and ε_0 is the vacuum permittivity. The thickness dependence of the dielectric constant was systematically investigated in Fig. 3d. For the 1000 μL samples, k increases from 1.96 at 32 nm to 3.49 at 54 nm, beyond which it saturates at approximately 3.49. For the 1500 μL samples, k increases from 3.68 at 43.6 nm to 5.40 at 66 nm, beyond which it saturates at approximately 5.4. The saturation regions are highlighted by gray shaded areas in Fig. 3d.

This saturation behavior indicates that the thickness dependence is not merely an artifact of series interfacial capacitance or measurement errors, but rather reflects an intrinsic microstructural feature of the carbonaceous network. We attribute this observation to the presence of sp^2 carbon clusters and polar oxygen-containing functional groups (C–O and C=O) dispersed within the dominant sp^3 carbon matrix (as confirmed by XPS, Fig. 2f). Below the threshold thickness, the film volume is insufficient to host a percolating network of these polarization-active species, and the measured effective k is suppressed by the low-k sp^3 matrix. Once the film thickness exceeds the critical value, the polarization-active species form a percolating network that enables full dipole polarization, and further thickness increase only adds inactive sp^3 carbon, resulting in a saturated k value. The different threshold values for the two concentrations (54 nm vs. 66 nm) reflect the different densities of polarization-active species in the precursor films,

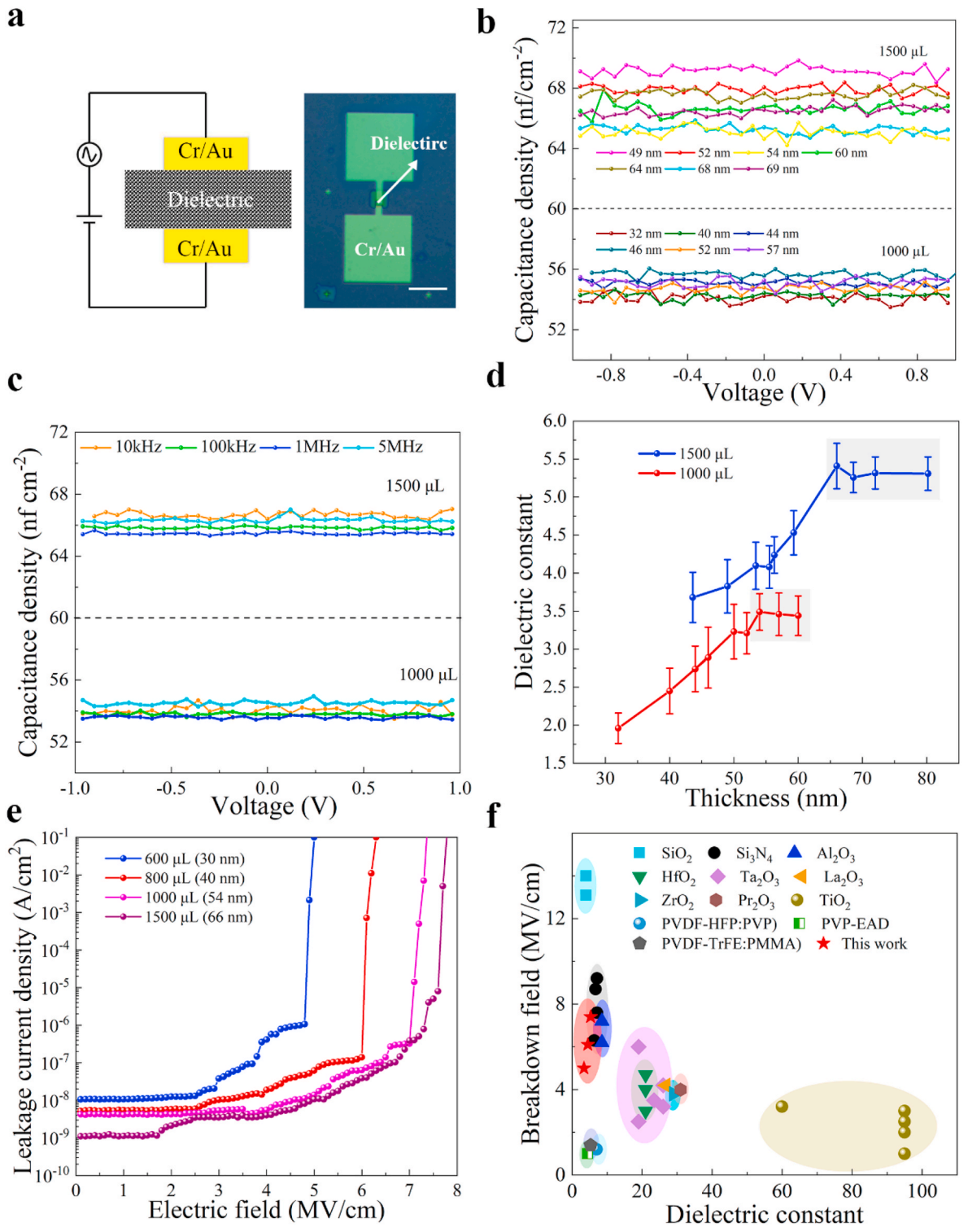

Fig. 3. a) Schematic diagram and an typical optical image of the MIM structures; Scale bars: 50 μm in the optical image. b) Capacitance–voltage (C–V) characteristics of MIM capacitors measured at 10 kHz for 1000 μL and 1500 μL samples with different dielectric thicknesses. c) Capacitance-voltage (C-V) characteristics of two carbon-based dielectrics fabricated with AZ5214 contents of 1500 μL and 1000 μL, measured at different frequencies (10 kHz, 100 kHz, 1 MHz, and 5 MHz). d) Thickness dependence of the dielectric constant k of carbon-based dielectrics fabricated with AZ5214 contents of 1500 μL and 1000 μL. e) Applied electric-field dependence of leakage current density in the carbon-based dielectrics fabricated with AZ5214 contents of 1500 μL, 1000 μL, 800 μL, and 600 μL; f) Breakdown electric field versus dielectric constant k for commonly used dielectric materials in conventional, 2D material, and organic FET processes [48–52].

which are determined by the initial AZ5214 concentration. The higher concentration (1500 μL) yields a more carbon-rich precursor, resulting in a higher density of sp^2 clusters and polar groups that require a larger thickness to establish a fully percolating network. Similar phenomena [54,55] have also been reported in other work settings.

To evaluate the dielectric robustness, we performed breakdown field measurements using a ramped voltage stress test on MIM capacitors with different AZ5214 concentrations (600, 800, 1000, and 1500 μL, 30 kV).

During the measurement, the bias voltage was continuously increased at a constant ramp rate while the leakage current was monitored in real time. The breakdown event was identified by a sudden and sharp increase in the slope of the leakage current–voltage curve (a clear inflection point indicating the onset of catastrophic conduction), and the electric field at this point was recorded as the breakdown field. The measurement range was extended up to 8 MV/cm to fully capture the breakdown behavior.

Fig. 3e presents the leakage current density as a function of the applied electric field for the four concentrations. The breakdown field increases monotonically with increasing AZ5214 concentration: 4.8 MV/cm for 600 μL, 6.1 MV/cm for 800 μL, 7.1 MV/cm for 1000 μL, and 7.4 MV/cm for the 1500 μL sample. For the optimized 1500 μL sample, the leakage current density remains as low as 7.8×10^{-7} A cm^{-2} at 7.3 MV cm^{-1}, just below the breakdown field, confirming the excellent insulating stability of the dielectric even under extreme electric field stress. This trend clearly demonstrates that a higher carbon source concentration leads to a more robust dielectric with superior breakdown resistance. The marked improvement in breakdown field with increasing AZ5214 concentration can be attributed to the enhanced carbonization and crosslinking density achieved at higher precursor concentrations. As confirmed by our XPS analysis (Fig. 2f), the resulting carbon network is predominantly sp^3-hybridized (64%), which provides a wide-bandgap insulating matrix that effectively suppresses carrier injection and avalanche breakdown. Furthermore, a higher precursor concentration yields a more densely packed and homogeneous carbon network after electron-beam irradiation, reducing the density of structural defects or pinholes that could serve as preferential pathways for electrical failure. The residual oxygen-containing functional groups (C–O and C=O, ~34%) also contribute to breakdown suppression by disrupting π-conjugated pathways and introducing deep trap states that impede charge transport.

Finally, in Fig. 3f, we compared the dielectric constant (k) and breakdown field (EBD) of our carbon-based dielectric with those of commonly used dielectric materials in conventional semiconductor FETs, two-dimensional FETs, and some organic FETs [48–52]. Our carbon-based dielectric exhibits a dielectric constant of ~5.4 and a breakdown field of 7.4 MV/cm, placing it in a competitive position among emerging dielectric materials. Notably, this performance is achieved through a simple, low-temperature, one-step electron-beam direct writing process, which offers several distinct advantages over conventional dielectric fabrication methods.

Compared with high-k oxides (HfO_2, Al_2O_3, Y_2O_3) grown by ALD or MBE, our e-beam direct writing approach eliminates the need for a seed layer and any graphene interface modification, thereby avoiding plasma-induced damage and reducing interface defects (Supporting Information Fig. S1) [56–58]. Moreover, it integrates material formation and patterning into a single step, simplifying the fabrication flow. Compared with polymer dielectrics, our carbon-based dielectric offers superior thermal stability and a higher breakdown field (7.4 MV/cm vs. 1–3 MV/cm). Its moderate k (≈5.4) strikes a favorable balance between gate controllability and leakage suppression—lower than high-k oxides but higher than most polymers (k ≈ 2–4) [22,59]. Compared with other carbon-based dielectrics (amorphous carbon, diamond-like carbon, carbon nitride, graphene oxide), our approach offers three key advantages: (i) a simple and scalable process (spin-coating + e-beam irradiation, no high-temperature annealing or transfer); (ii) direct-write patterning without additional lithography or etching; and (iii) a structurally engineered sp^3-dominated network (64%) with oxygen functionalities (34%) that ensures excellent insulation with tunable thickness and capacitance.

Crucially, the small gate capacitance of our dielectric—lower than most high-k oxides—provides three benefits for device applications [60–62]: (i) enhanced maximum oscillation frequency (fmax) in RF/terahertz devices via reduced RC delay; (ii) lower dynamic power consumption in logic switching; and (iii) improved sensitivity in chemical/biosensors, where transconductance is inversely proportional to gate capacitance. Combined with its high breakdown field and frequency stability up to 5 MHz, our electron-beam-written carbon-based dielectric stands as a promising candidate for next-generation electronic devices.

3.3. Graphene-based top-gated FETs with carbon-based dielectric

To validate the performance of carbon-based dielectric in graphene-based devices, a graphene top-gated FET was fabricated by using epitaxial graphene as the channel and a 44.7-nm-thick carbon-based dielectric fabricated from 1000 μL AZ5214 content as the top-gate dielectric layer. The single-layer graphene used in the FET was epitaxially grown on the Si face of 4H-SiC with n-doping, and its Raman spectra, AFM, and lateral force microscopy (LFM) results are shown in the supporting information Fig.S2.

After patterning the epitaxial graphene on the Si face of 4H-SiC by photolithography, a 10-μm-wide and 30-μm-long graphene channel was obtained, followed by fabricating drain and source electrodes (20 nm Cr/20 nm Au). The patterned carbon dielectric layer was developed via electron-beam direct writing of AZ5214 photoresist. Finally, a gate electrode (20 nm Cr/20 nm Au) with a width of 7 μm was prepared to complete the preparation of the graphene-based FET. The device structure and a typical SEM image are shown in Fig. 4a, where the patterned carbon dielectric is placed on the black area.

The transfer and output characteristics of the graphene-based FET are shown in Fig. 4b and e, respectively. From the transfer curve in Fig. 4b, the charge neutrality point (the minimum of the channel current) is observed at $V_g = -3.5$ V, indicating n-type doping behavior. The corresponding transconductance ($g_m = dI_d/dV_g$) is presented in Fig. 4c, where a maximum value of 7.3 mS/mm is achieved at $V_d = 4$ V. Notably, the transconductance on the hole side (i.e., for gate voltages above the charge neutrality point) remains approximately constant over a wide gate voltage range, indicating good electrostatic control and a clean graphene/dielectric interface. The extracted carrier mobility is 2607 cm^2/(V·s), which is competitive with values reported for graphene FETs utilizing other dielectric materials. Importantly, the gate leakage current remains consistently below 15 pA throughout the entire gate voltage sweep (Fig. 4d), confirming that leakage through the carbon-based dielectric does not interfere with the transfer characteristic measurement. As shown in Fig. 4e, the output characteristics exhibit no clear current saturation up to $V_d = 10$ V, suggesting that the transconductance will continue to increase with increasing drain voltage.

Finally, we compared FETs with graphene channels obtained using different methods (i.e., epitaxy, CVD-growth, and exfoliation) and different dielectric materials as the dielectric layer [63–72]. The relationship between the dielectric constant k of the dielectric material and the mobility μ of the device was plotted in Fig. 4d. The fabricated gate dielectric (k = 2.8) achieves an excellent carrier mobility of 2607 cm^2/(V·s) in graphene top-gated field-effect transistors, striking a superior balance between dielectric constant and transport performance. Unlike high-k materials such as HfO_2 (k > 17) which often severely degrade mobility, or low-k SiO_2 (k ≈ 3.9) which offers weaker electrostatic control, the present dielectric maintains a moderate k value while preserving high mobility, indicating low interface scattering and defect density. Moreover, this performance is obtained without complex buffer layers or specialized processing, demonstrating good compatibility with standard semiconductor fabrication. These combined features—balanced dielectric constant, high mobility, clean graphene/dielectric interface, and process simplicity—make this gate dielectric a highly promising candidate for practical graphene top-gated FETs.

4. Conclusions

In this work, we have developed a high-performance carbon-based dielectric fabricated by electron-beam direct writing of AZ5214

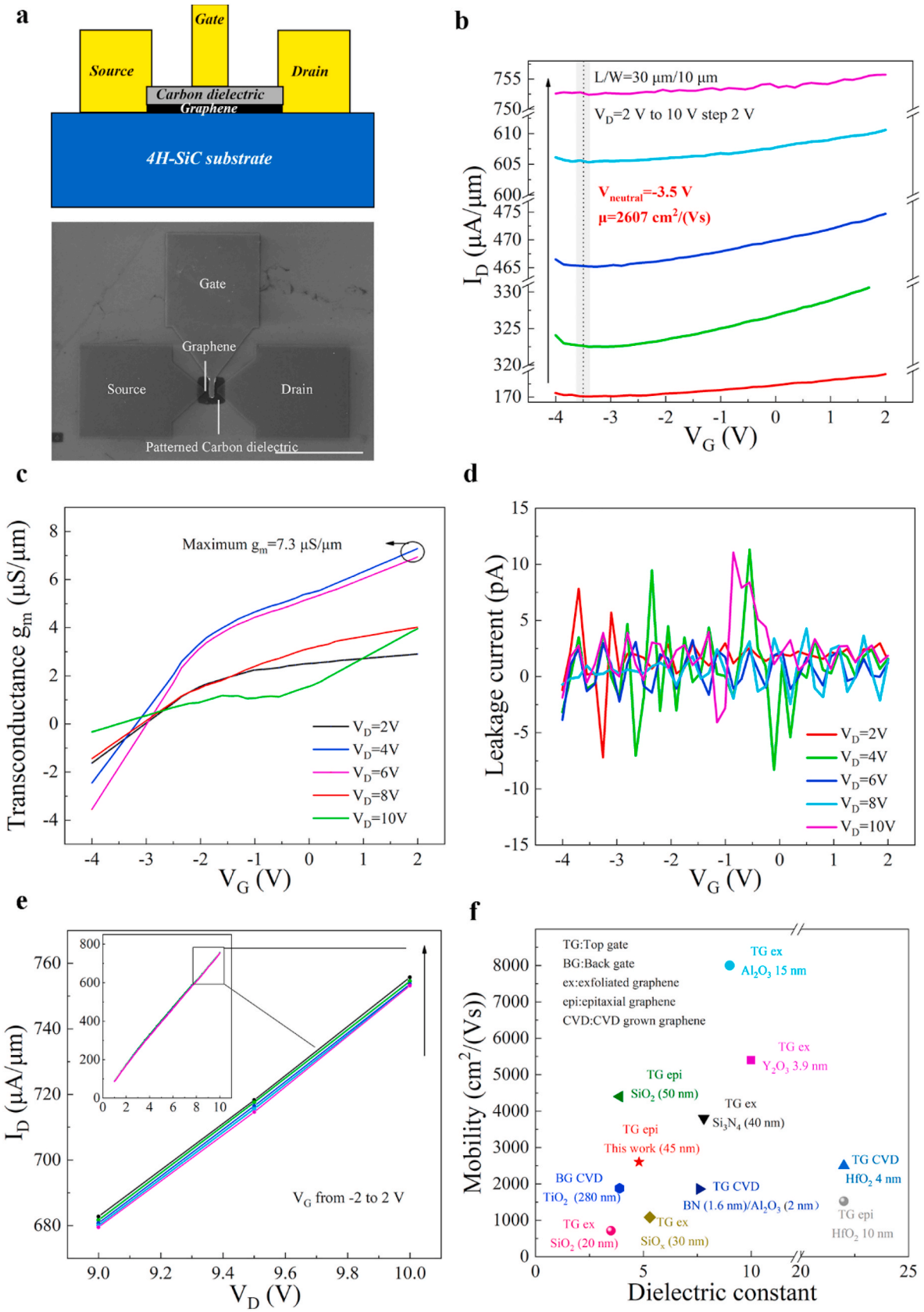

Fig. 4. a) Schematic diagram and SEM image of a typical top-gated FET with carbon-based dielectrics as the top-gate dielectric layer and epitaxial graphene as the channel, the scale is 100 μm. b) Transfer characteristics, c) Transconductance g_m versus gate voltage V_G and d) Leakage current versus V_G of a top-gated FET with a carbon-based dielectric and a 30 × 10 μm epitaxial graphene channel. f) Mobility μ versus dielectric constant k for FETs with graphene channels grown by various approaches and dielectric layers of different materials [63–72].

photoresist. The electron-beam irradiation induces crosslinking and partial carbonization, forming a disordered carbonaceous network with a predominantly sp^3-hybridized framework (64%), minimal sp^2 fraction (2.04%), and substantial oxygen-containing functional groups (~34%), as confirmed by XPS. This unique chemical structure provides the fundamental basis for the excellent insulating behavior of the material. The dielectric exhibits a dielectric constant of ~5.4, a high breakdown field of 7.4 MV/cm, frequency-stable response up to 5 MHz, and voltage-independent capacitance. When integrated as the gate dielectric in top-gated graphene FETs, it achieves a carrier mobility of 2607 $cm^2/(V{\cdot}s)$, demonstrating a clean and low-defect interface without the need for seed layers or surface modification.

Beyond its balanced dielectric performance and high mobility, our electron-beam direct writing approach offers several distinct advantages: (i) simple, scalable fabrication without high-temperature annealing or post-deposition transfer; (ii) direct-write patterning that eliminates additional lithography and etching; (iii) damage-free processing that preserves channel quality; and (iv) precise thickness control for tunable capacitance. Its moderate dielectric constant yields a small gate capacitance, beneficial for high-frequency operation, low-power logic, and high-sensitivity sensing. These combined features establish the electron-beam-written carbon-based dielectric as a promising candidate for next-generation carbon-based electronics.

CRediT authorship contribution statement

Rui Li: Writing – original draft, Methodology, Investigation, Data curation. **Hao Tian:** Data curation. **Kaicheng Yu:** Data curation. **Cao Tang:** Data curation. **Kaiming Zhang:** Data curation. **Luzhen Hao:** Data curation. **Xin He:** Writing – review & editing. **Yanqing Ma:** Writing – review & editing, Funding acquisition. **Lei Ma:** Writing – review & editing, Supervision, Methodology, Investigation, Funding acquisition, Formal analysis, Data curation.

Declaration of competing interest

The authors declare that they have no known competing financial interests or personal relationships that could have appeared to influence the work reported in this paper.

Acknowledgments

This work was financially supported by the National Key R&D Program of China (No. 2022YFC3006303), Tianjin National Science Foundation Project (No. 25JCZDJC01380) and the Innovation fund of Haihe Laboratory of Low-dimensional Electronic Materials (25HHDWSS00002, 25HHDWSS00005).

Appendix A. Supplementary data

Supplementary data to this article can be found online at https://doi.org/10.1016/j.mssp.2026.111125.

Data availability

Data will be made available on request.

References

[1] G.E. Moore, Cramming more components onto integrated circuits, IEEE Solid State Circuits Soc. Newslett. 38 (11) (1965) 114-117.
[2] G.E. Moore, Progress in digital integrated electronics. International Electron Devices Meeting 3, IEEE, 1975, pp. 11–13.
[3] Q. Cao, Carbon nanotube transistor technology for More-Moore scaling, Nano Res. 14 (9) (2021) 3051–3069.
[4] T. Srimani, G. Hills, M. Bishop, et al., Heterogeneous integration of BEOL logic and memory in a commercial foundry: multi-tier complementary carbon nanotube logic and resistive RAM at a 130 nm node, in: 2020 Symposium on VLSI Technology Digest of Technical Papers, 20, 2020, 978-971-7281-6460-7281.
[5] H. Xu, L. Peng, Carbon-based integrated circuit technology: development and forecast, Front. Data Comput. 3 (2021) 4–27.
[6] S. Rodriguez, A. Rusu, J M d l Rosa, Overview of carbon-based circuits and systems. Proceedings-IEEE International Symposium on Circuits and Systems, 2015, pp. 2912–2915.
[7] C. Berger, Z. Song, X. Li, et al., Electronic confinement and coherence in patterned epitaxial graphene, Science 312 (5777) (2006) 1191–1196.
[8] J. Liang, Y. Chen, Y. Xu, et al., Toward all-carbon electronics: fabrication of graphene-based flexible electronic circuits and memory cards using maskless laser direct writing, ACS Appl. Mater. Interfaces 2 (11) (2010) 3310–3317.
[9] H.-Q. Wu, C.-Y. Linghu, H.-M. LU, et al., Graphene applications in electronic and optoelectronic devices and circuits, Chin. Phys. B 22 (9) (2013), 098106-098116.
[10] Y. Wu, D.B. Farmer, F. Xia, et al., Graphene electronics: materials, devices, and circuits, Proc. IEEE 101 (7) (2013) 1620–1637.
[11] S. Lijima, Helical microtubules of graphitic carbon, Nature 354 (1991) 737–740.
[12] L.-M. Peng, Z. Zhang, C. Qiu, Carbon nanotube digital electronics, Nat. Electron. 2 (11) (2019) 499–505.
[13] A.D. Franklin, Nanomaterials in transistors: from high-performance to thin-film applications, Science 349 (6249) (2015) aab2750-2759.
[14] F. Schwierz, Graphene transistors, Nat. Nanotechnol. 5 (7) (2010) 487–496.
[15] A. Fan, Q. Zhang, Y. Wang, et al., Recent advances in layer engineering and controllable fabrication of graphene, h-BN, and transition metal dichalcogenides, Sci. China Mater. 68 (9) (2025) 3143–3170.
[16] K. Agashiwala, A. Kumar, L. Xu, et al., CMOS-compatible pressure-assisted solid-phase-diffusion technique for large-area multilayer graphene synthesis, Small 21 (28) (2025) e2400128-e2400139.
[17] F. Zouaoui, G. Menassol, C. Ducros, et al., Electrochemical sensors based on amorphous carbon electrode: a review, Microchem. J. (2025) 209, 112345-112359.
[18] I.S. Kim, C.E. Shim, S.W. Kim, et al., Amorphous carbon films for electronic applications, Adv. Mater. 35 (43) (2023) e2204912-e2204925.
[19] J. Kang, D. Sarkar, Y. Khatami, et al., Proposal for all-graphene monolithic logic circuits, Appl. Phys. Lett. 103 (8) (2013), 083113-083117.
[20] F. Al-Dirini, F.M. Hossain, A. Nirmalathas, et al., All-graphene planar self-switching MISFEDs, metal-insulator-semiconductor field-effect diodes, Sci. Rep. 4 (2014) 3983-3991.
[21] S. Lee, K. Lee, C.-H. Liu, et al., Flexible and transparent all-graphene circuits for quaternary digital modulations, Nat. Commun. 3 (2012) 1018-1026.
[22] D.-M. Sun, M.Y. Timmermans, A. Kaskela, et al., Mouldable all-carbon integrated circuits, Nat. Commun. 4 (2013) 2302-2310.
[23] B.J.L.S.K. Kim, M.S. Kang, Coplanar-gate transparent graphene transistors and inverters on plastic, ACS Nano 6 (10) (2012) 8646–8651.
[24] K. Zhang, N. Gao, J. Zhang, et al., Boosting carbon nanotube transistors through gamma-ray irradiation, Nat. Commun. 17 (1) (2026,125-134).
[25] F. Giannazzo, E. Schilirò, R. Lo Nigro, et al., Atomic layer deposition of High-k insulators on epitaxial graphene: a review, Appl. Sci. 10 (7) (2020, 2583-2605).
[26] S. Yang, K. Liu, Y. Xu, et al., Gate dielectrics integration for 2D electronics: challenges, advances, and outlook, Adv. Mater. 35 (18) (2023) e2207901-e2207922.
[27] X. Yang, Y. Yang, S. Cheng, et al., Conformal hexagonal boron nitride encapsulation of graphene-skinned glass fiber fabric for enhanced electrical stability, Nat. Commun. 16 (1) (2025) 4965-4977.
[28] H. Li, Y. Tang, W. Guo, et al., Polyfluorinated electrolyte for fully printed carbon nanotube electronics, Adv. Funct. Mater. 26 (38) (2016) 6914–6920.
[29] Y. Liu, F. Wang, X. Wang, et al., Planar carbon nanotube-graphene hybrid films for high-performance broadband photodetectors, Nat. Commun. 6 (2015) 8589-8598.
[30] W.F. Van Dorp, C.W. Hagen, A critical literature review of focused electron beam induced deposition, J. Appl. Phys. 104 (8) (2008), 081301-081320.
[31] G d Boer, M.P. Dansberg, R. Jager, et al., MAPPER: progress toward a high-volume manufacturing system [Z]. Alternative Lithographic Technologies V, 2013, https://doi.org/10.1117/12.2011486, 86800A-86800A-12.
[32] F. Klein, U. Treske, A. Koitzsch, et al., Nanoscale scanning electron microscopy based graphitization in tetrahedral amorphous carbon thin films, Carbon 107 (2016) 536–541.
[33] W. Chen, Y. Yu, X. Zheng, et al., All-carbon based graphene field effect transistor with graphitic electrodes fabricated by e-beam direct writing on PMMA, Sci. Rep. 5 (2015) 12198-12206.
[34] R. Du, S. Ssenyange, M. Aktary, et al., Fabrication and characterization of graphitic carbon nanostructures with controllable size, shape, and position, Small 5 (10) (2009) 1162–1168.
[35] A. Garcia-Serrano, S. Sangtarash, A. Gonzalez-Orive, et al., Molecular electronics meets direct-write carbon nanofabrication via focused electron-beam-induced deposition (FEBID): a platform for junction architecture design, ACS Appl. Electron. Mater. 7 (20) (2025) 9470–9479.
[36] K. Bi, J. Mu, W. Geng, et al., Reliable fabrication of graphene nanostructure based on e-Beam irradiation of PMMA/Copper composite structure, Materials (Basel) 14 (16) (2021, 4602-4613).
[37] H. Gao, V. Belova, F.L. Porta, et al., Graphene at liquid copper catalysts: atomic-scale agreement of experimental and first-principles adsorption height, Adv. Sci. (Weinh.) 9 (36) (2022) e2204684-e2204693.
[38] G. Papadimitropoulos, S. Cibella, R. Leoni, et al., Fabrication of Micro- and Nanoelectrodes by Selective Chemical Vapor Deposition of Cu on Si Substrates Patterned with AZ5214 and PMMA, ECS Meet Abstr. (2009). MA2009-02: 2669–2669.

[39] S. Aikawa, T. Kizu, E. Nishikawa, Catalytic graphitization of an amorphous carbon film under focused electron beam irradiation due to the presence of sputtered nickel metal particles, Carbon 48 (10) (2010) 2997–2999.
[40] W.F.V.S.B. Van Dorp, C.W. Hagen, Approaching the resolution limit of nanometer-scale electron beam-induced deposition, Nano Lett. 5 (7) (2005) 1303–1307.
[41] S.J. Randolph, J.D. Fowlkes, P.D. Rack, Focused, nanoscale electron-beam-induced deposition and etching, Crit. Rev. Solid State Mater. Sci. 31 (3) (2007) 55–89.
[42] J. Skriniarováa, D. PudiSb, R. Andokc, et al., Investigation of the AZ 5214E photoresist by the laser interference, EBDW and NSOM lithographies, Appl. Surf. Sci. 395 (2017) 226–231.
[43] D.D. Kulkarni, K. Rykaczewski, S. Singamaneni, et al., Thermally induced transformations of amorphous carbon nanostructures fabricated by electron beam induced deposition, ACS Appl. Mater. Interfaces 3 (3) (2011) 710–720.
[44] I.F.J.E.F. Zailer, V. Chabasseur-Molyneux, Crosslinked PMMA as a high-resolution negative resist for electron beam lithography and applications for physics of low-dimensional structures, Semicond. Sci. Technol. 11 (8) (1996) 1235–1238.
[45] A. Pandey, S. Maity, D. Bandyopadhyay, et al., Self-organization of random copolymers to nanopatterns by localized e-beam dosing, Nanotechnology 32 (28) (2021), 285301-285312.
[46] H. Duan, J. Zhao, Y. Zhang, et al., Preparing patterned carbonaceous nanostructures directly by overexposure of PMMA using electron-beam lithography, Nanotechnology 20 (13) (2009) 135306-135315.
[47] J.R.A.F.A. C, Interpretation of Raman spectra of disordered and amorphous carbon, Phys. Rev. B 61 (20) (2000) 14095–14107.
[48] H. Palneedi, M. Peddigari, G.-T. Hwang, et al., High-performance dielectric ceramic films for energy storage capacitors: progress and outlook, Adv. Funct. Mater. 28 (42) (2018), 1803665-1803685.
[49] J. Mcpherson, J. Kim, A. Shanware, et al., Proposed universal relationship between dielectric breakdown and dielectric constant, Tech. Digest Int. Elect. Devices Meet. (2002) 633–636.
[50] C. Lu, W.-Y. Lee, C.-C. Shih, et al., Stretchable polymer dielectrics for low-voltage-driven field-effect transistors, ACS Appl. Mater. Interfaces 9 (30) (2017) 25522–25532.
[51] K.-J. Baeg, D. Khim, J. Kim, et al., Controlled charge transport by polymer blend dielectrics in top-gate organic field-effect transistors for low-voltage-operating complementary circuits, ACS Appl. Mater. Interfaces 4 (11) (2012) 6176–6184.
[52] M.E. Roberts, N. Queraltó, Water-stable organic transistors and their application in chemical and biological sensors, Proc. Natl. Acad. Sci. U. S. A 105 (34) (2008) 12134–12139.
[53] Z. Jinbiao, S. Fangwu, Microwave measurement of complex dielectric constant, J. Electron. 5 (4) (1988) 312–317.
[54] J. Yuan, C. Jian, Y. Gong, et al., High-κ samarium oxysulfate dielectric for two-dimensional electronics with enhanced gate coupling, Nat. Commun. 17 (1) (2025, 215-226).
[55] D.S. Boesch, J. Son, J.M. Lebeau, et al., Thickness dependence of the dielectric properties of epitaxial SrTiO3Films on (001)Pt/SrTiO3, APEX 1 (2008), 091601-091604.
[56] H. Yang, W. Chen, M.-Y. Li, et al., Ultrathin Al oxide seed layer for atomic layer deposition of High-κ Al2O3 dielectrics on graphene, Chin. Phys. Lett. 37 (7) (2020), 077301-077305.
[57] W. Li, J. Zhou, S. Cai, et al., Uniform and ultrathin high-κ gate dielectrics for two-dimensional electronic devices, Nat. Electron. 2 (12) (2019) 563–571.
[58] J. Kim, S. Jandhyala, Atomic layer deposition of dielectrics for carbon-based electronics, Thin Solid Films 546 (2013) 85–93.
[59] B.J. Kim, S.-K. Lee, M.S. Kang, et al., Coplanar-gate transparent graphene transistors and inverters on plastic, ACS Nano 6 (2012) 8646–8651.
[60] F. Xia, T. Xia, H. Su, et al., Flexible radio-frequency carbon nanotube transistors operating at frequencies above 100 GHz, Nat. Electron. (2026, in press).
[61] C.D. Pham, Q.T. Trinh, J. Zhang, et al., Pushing biomolecule detection limit with graphene field-effect transistor biosensors, Adv. Electron. Mater. 11 (19) (2025), 2400892-2400905.
[62] S.L. Li, H. Miyazaki, A. Kumatani, et al., Low operating bias and matched input-output characteristics in graphene logic inverters, Nano Lett. 10 (7) (2010) 2357–2362.
[63] Y.M. Lin, C. Dimitrakopoulos, K.A. Jenkins, et al., 100-GHz transistors from wafer-scale epitaxial graphene, Science 327 (5966) (2010) 662-665.
[64] S. Kim, J. Nah, I. Jo, et al., Realization of a high mobility dual-gated graphene field-effect transistor with Al2O3 dielectric, Appl. Phys. Lett. 94 (6) (2009), 062107-062110.
[65] M.C. Lemme, T.J. Echtermeyer, M. Baus, et al., A graphene field-effect device, IEEE Electron Device Lett. 28 (4) (2007) 282–284.
[66] Y.Q. Wu, P.D. Ye, M.A. Capano, et al., Top-gated graphene field-effect-transistors formed by decomposition of SiC, Appl. Phys. Lett. 92 (9) (2008), 092102-092105.
[67] O. Habibpour, S. Cherednichenko, J. Vukusic, et al., Mobility improvement and microwave characterization of a graphene field effect transistor with silicon nitride gate dielectrics, IEEE Electron Device Lett. 32 (7) (2011) 871–873.
[68] Xu Z.Z. Huilong, Haitao Xu, Zhenxing Wang, Sheng Wang, Lian-Mao Peng, Top-gated graphene field-effect transistors with high normalized transconductance and designable dirac point voltage, ACS Nano 5 (6) (2011) 5031–5037.
[69] M. Xiao, C. Qiu, Z. Zhang, et al., Atomic-layer-deposition growth of an ultrathin HfO_2 film on graphene, ACS Appl. Mater. Interfaces 9 (39) (2017) 34050–34056.
[70] L. Yang, H. Wang, X. Zhang, et al., Thermally evaporated SiO serving as gate dielectric in graphene field-effect transistors, IEEE Trans. Electron. Dev. 64 (4) (2017) 1846–1850.
[71] P.A. Flores-Silva, C. Borja-Hernández, C. Magaña, et al., Graphene field effect transistors using TiO_2 as the dielectric layer, Phys. E Low-dimens. Syst. Nanostruct. (2020) 124, 114334-114341.
[72] M. Snure, S.R. Vangala, T. Prusnick, et al., Two-dimensional BN buffer for plasma enhanced atomic layer deposition of Al_2O_3 gate dielectrics on graphene field effect transistors, Sci. Rep. 10 (1) (2020) 1469914708.